Journal of Materials Chemistry A

Accepted Manuscript

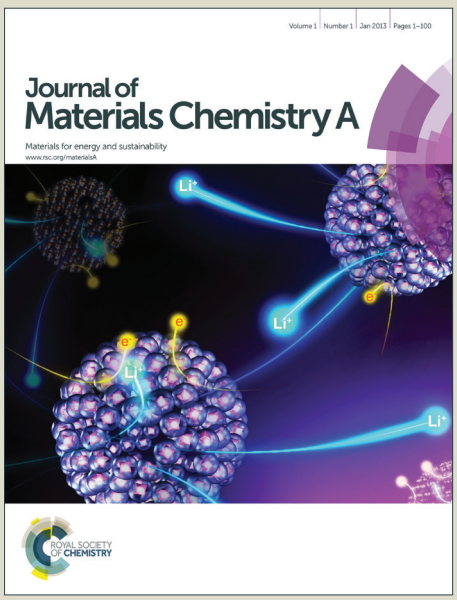

ROYAL SOCIETY OF CHEMISTRY

www.rsc.org/materialsA

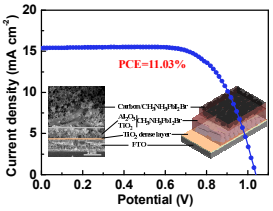

Efficient $CH_3NH_3PbI_2Br$ perovskite solar cells have been prepared based on TiO_2/Al_2O_3/carbon architecture, yielding an appreciated power conversion efficiency of 11.03%.

Cite this: DOI: 10.1039/c0xx00000x

www.rsc.org/xxxxxx

ARTICLE TYPE

Efficient Mesoscopic Perovskite Solar Cells based on $CH_3NH_3PbI_2Br$ Light Absorber

Kun Cao,[a] Jin Cui,[a] Hua Zhang,[a] Hao Li,[a] Jinkui Song,[a] Yan Shen,[a] Yibing Cheng[b] and Mingkui Wang*[a]

Received (in XXX, XXX) Xth XXXXXXXXX 20XX, Accepted Xth XXXXXXXXX 20XX
DOI: 10.1039/b000000x

Efficient mesoscopic $CH_3NH_3PbI_2Br$ perovskite solar cells have been prepared based on the TiO_2/Al_2O_3/carbon architecture. An appreciated power conversion efficiency of 11.03% was achieved under AM 1.5G illumination. This system combines the superior stability of $MAPbI_2Br$ and no requirement of hole conductor layer.

Introduction

Hybrid lead-halide perovskite solar cells (PSC) have been demonstrated as one of the most promising and fastest growing photovoltaic technologies.[1-3] Since the first introduction in 2009, solar cells using these materials have evolved rapidly to yield unprecedented overall power conversion efficiency (PCE) of over 20%.[4] The most commonly used perovskite is $CH_3NH_3PbI_3$ (CH_3NH_3 abbreviated as MA hereafter).[5-7] However, the mixed halide $MAPb(I_{1-x}Cl_x)_3$ and $MAPb(I_{1-x}Br_x)_3$ analogues by partial substitution with chlorine and bromine have been widely investigated, which are supposed to be chemically stable in conjunction with humidity resistance.[8-14] It is found that the optical band gap of halide perovskite can be able to tune from about 1.5 to 2.2 eV by varying the halide composition between iodide and bromide in this material.[15-17] Seok *et al.* firstly demonstrated the deposition of $MAPb(I_{1-x}Br_x)_3$ (especially for the composition where x=0~0.2) in mesoporous TiO_2 films with reasonable device performance.[16] Their work showed an improved stability of $MAPb(I_{1-x}Br_x)_3$ ($x \geq 0.2$) device compared to that of $MAPbI_3$ under the same humidity conditions. It was ascribed to the substitution of larger I atoms with smaller Br atoms in $MAPb(I_{1-x}Br_x)_3$, leading to the reduction of the lattice constant and a transition to a cubic phase.[16] Among these perovskites, $MAPbI_2Br$ has a high absorption coefficient in visible light region (400-700 nm) together with its prolonged charge carrier lifetime, which makes it a promising candidate for developing stable perovskite solar cells with high-efficiency. Moreover, the $MAPbI_2Br$ has also been found to have an upper conduction band (CB) position, enabling a greater driving force to inject electrons into the CB of the TiO_2. However, so far only a few papers have reported on mesoporous PSC based on $MAPbI_2Br$. Qiu *et al.* reported a PSC device with a power conversion efficiency (PCE) of 5% by using the TiO_2 NWAs as electron transport material (ETM) and $MAPbI_2Br$ as absorber.[18] A higher V_{OC} could be achieved with this device than that based on the analogue $MAPbI_3$. Very recently, Zhang and co-workers reported a PSC with 6.64% PCE using $MAPbI_2Br$ as light absorber and poly(3-hex-ylthiophene) (P3HT) as hole-transporting layer.[19] It is found in these cells photovoltage is usually limited to ~0.8 V, which is not in accordance with the expectation that larger open-circuit voltages could be achieved by using the mixed-halide perovskites with large bandgaps.[20] This may be attributed to the factor related to the deposition of high-quality $MAPbI_2Br$ perovskites, resulting in the probability of recombination at the interfaces between the electron conductor and pervoskite as well as hole conductor and perovskite. Recently, Zhao *et al.* reported a planar $MAPbI_2Br$-based PSC device with spiro-MeOTAD as hole extraction layer, showing ~10% efficiency.[21] The uniform compact perovskite layer was fabricated with thermal decomposition from a precursor containing MACl as a glue or soft template.[21,22]

Perovskite crystallization from solution produces large morphological variations and incomplete filling of the mesoporous oxide scaffold, which results in an unwanted spread of the photovoltaic performance of the resulting devices.[23-25] For instance, the charge recombination happened at the interfaces between perovskite/selective contact materials, as well as the charge transfer between ETM and the back contact in these typical device structures is the main reason which restricts the efficiency of $MAPbI_2Br$-based PSC devices.

In this communication, we present on mesoscopic PSC devices using $MAPbI_2Br$ as light absorber. The metal halide perovskite is infiltrated into the mesoporous oxide scaffold by drop-coating deposition through the porous carbon layer.[23,26] Compared to the planar structure devices the crystallization of the perovskite is constraint within the mesopores in the oxides scaffold. Photo-generated holes transport directly to the counter electrode since metal halide perovskite can act as hole conductor as well. When a triple-layer of mesoscopic TiO_2/Al_2O_3/carbon is employed as scaffold and infiltrated with $MAPbI_2Br$, an overall energy conversion of 11.03% with an impressive photovoltage over 1.10 V was achieved under standard AM 1.5 illumination at 100 mW cm^{-2}. This system combines the superior stability of $MAPbI_2Br$ and no requirement of high-cost HTMs and much simply manufacture process.

Experimental Section

Material synthesis

CH_3NH_3I and CH_3NH_3Br were synthesized by reacting 30 mL of methylamine (40% in methanol, TCI) and 32.3 mL of hydroiodic acid (57 wt% in water, Aldrich) or 23.32 mL of hydrobromic acid (48 wt% in water, Aldrich) in a 250 mL round bottom flask at 0 °C for 2 h with stirring. The precipitate was recovered by putting the solution on a rotavap and carefully removing the solvents at 50 °C. The product of methylammonium iodide (CH_3NH_3I) or methylammonium bromide (CH_3NH_3Br) was washed with ethanol by stirring the mixture for 30 min. Then, the mixture was filtered and washed three times with diethylether. After filtration, the solid was collected and dried at 70 °C in a vacuum oven for 40 h.

Device fabrication

Devices were fabricated on fluorine doped tin oxide (FTO) coated glass serving as transparent electrode and substrate, respectively. A compact layer of TiO_2 was deposited on the cleaned FTO glass by spray pyrolysis deposition with di-isopropoxytitanium bis(acetyl acetonate) solution at 450 °C. Al_2O_3 pastes used for screen printing was prepared by mixing 3 g of Al_2O_3 nanopowder (alladin, 20 nm) in 80 ml ethanol and subsequently adding with 15 g of 10 wt% ethyl cellulose (in EtOH) and 10 g of terpineol. A 400 nm mesoporous TiO_2 films based on commercially available precursor pastes (DSL. 18NR-T, 20 nm, Dyesol, Austrilia, diluted at 1/3.5 mass ratio of paste/terpilenol), a 600 nm Al_2O_3 and a 10 μm carbon black/graphite layer were subsequently prepared by screen printing onto FTO conducting glass layer by layer, which were sintered at 500 °C for 30 min. The thickness of each layer was measured by profile-system (DEKTAK, VEECCO, Bruker). The device structure were sintered at 400 °C for 30 min and then cooled to room temperature. After that, the resulted films were infiltrated with PbI_2 by dropping a PbI_2 solution in DMF (500 mg ml^{-1}) that was kept at 70 °C. After drying, the films were dipped into methylammonium solution (10 mg ml^{-1}) and the films changed color from light yellow to black during the dipping process, indicating the formation of the perovskite.

Devices characterization

Film cross sections were obtained using an FEI Magellan-400 field emission scanning electron microscope (FESEM). The time-resolved luminescence decays were recorded with Edinburgh instruments (FLSP920 spectrometers). The excitation light source was a picosecond pulsed light-emitting diodes centered at 445 nm, operated at a frequency of 10 MHz. A xenon light source solar simulator (450W, Oriel, model 9119) with AM 1.5G filter (Oriel, model 91192) was used to give an irradiance of 100 mW cm^{-2} at the surface of the solar cells. Various irradiance intensities from 0.01 to 1.0 sun can be provided with neutral wire mesh attenuators, and the light intensity was calibrated with a standard silicon solar cell. The current-voltage characteristics of the devices under these conditions were obtained by applying external potential bias to the devices and measuring the generated photocurrent with a Keithley model 2400 digital source meter. A similar data acquisition system was used to control the incident photon-to-current conversion efficiency (IPCE) measurement. The devices were tested using a metal mask with an aperture area of 0.16 cm^2 to prevent the scattering light.

Results and discussion

The XRD patterns for $MAPbI_2Br$ and $MAPbI_3$ films are shown in Fig. 1a. This result indicates that both materials have a similar crystalline structure assignable to the perovskite system. Compared to $MAPbI_3$, the diffraction peaks of $MAPbI_2Br$ are shifted uniformly to higher angles, which can be rationalized by the shrunken crystalline lattice wholly caused by the single-atom replacement of I with Br. The single peak at 28.88° (Fig. S1) is a key indication of a cubic perovskite phase as previously reported.[18] These atomic to structural changes in the material result in important variations in its optical and electronic properties, thereby offering a handle to modulate the photovoltaic operation of the perovskite devices. The UV/Vis absorbance spectrum can tell us the light absorbing property of the perovskite. As shown in Fig. 1b, the $MAPbI_2Br$ film exhibits an onset absorption band at around 700 nm, while the $MAPbI_3$ absorbs light in a relatively longer wavelength region up to ~ 800 nm. The different absorption ranges can be easily ascribed to the variation of the energy band gaps (Eg) of those two semiconductor absorbers, arising from the Br-replacement induced structural modifications. It is reported that the $MAPbI_2Br$ perovskite with a wider band gap (~1.77 eV) than $MAPbI_3$ (~1.55 eV), which is in accordance with the absorption spectrum.[17] The corresponding PL spectrum of the $MAPbI_2Br$ film is shown in Fig. S2. An obvious emission peak of $MAPbI_2Br$ at around 700 nm is observed, showing a little Stocks shift in comparison with the absorbance spectrum.

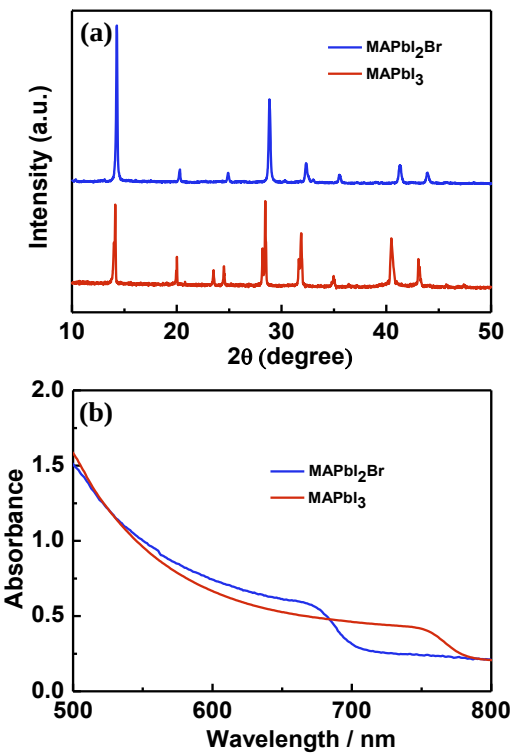

Fig. 1 XRD patterns and (b) UV/Vis absorption spectra of the $MAPbI_2Br$ film and $MAPbI_3$ film deposited on glass substrates

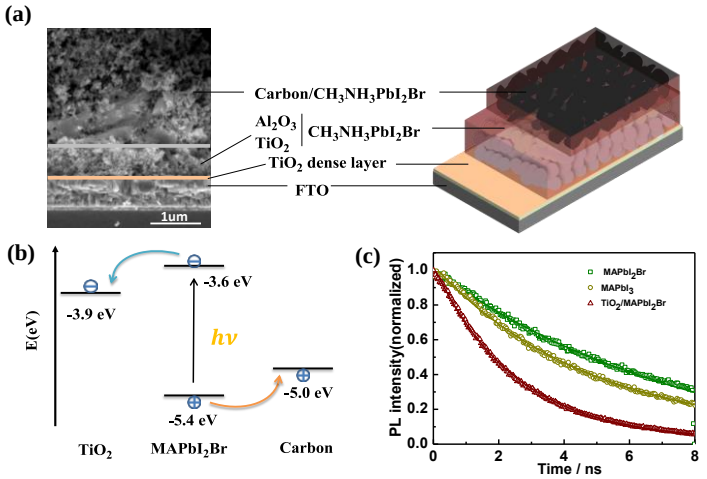

Fig. 2 (a) Cross-sectional SEM image and Schematic illustration of the triple-layered printable perovskite solar cell. (b) Approximate energy band diagram of the fabricated device configuration. (c) Time-resolved PL decay detected at peak wavelength of emission for $MAPbI_2Br$, $MAPbI_3$, and $TiO_2/MAPbI_2Br$.

The schematic structure of a typical mesoscopic PSC is shown in Fig. 2a. All the films including the mesoporous layers of TiO_2 and Al_2O_3 with a total thickness of ~1μm are demonstrated in the cross section SEM image of the device as given in Fig. 2a. The mesoscopic carbon CE with a thickness of ~10 μm was screen-printed on to mesoscopic oxide layers. In this study, the mesoporous layers were infiltrated with $MAPbI_2Br$ by the drop-coating method combined with sequential deposition technique, which is proved successful in producing mixed Br/I perovskites.[17] The PbI_2 was firstly deposited by drop-casting from solution through mesoporous carbon layer and subsequently transformed into the perovskite by exposing the whole device to a solution of CH_3NH_3Br (see experiments for details). The perovskites are partially filled in the carbon electrode as observed in the SEM image in Fig. 2a, which yields an interpenetrating interface between perovskite and the counter electrode. Therefore, a low contact resistance would be expected for this optimized interface, which might result in a high photovoltaic performance compared with the system having the perovskites only in the oxide layers.[27] The energy level in Fig. 2b allows electron extraction from $MAPbI_2Br$ (-3.6 eV) to TiO_2 (-3.9 eV) conduction band, and hole collection from $MAPbI_2Br$ valence band (-5.4 eV) to carbon CE (-5.0 eV). The PL quenching effect of TiO_2 can be observed in the time-resolved PL decay plot as shown in Fig. 2c. The presences of TiO_2 layer dramatically accelerate the PL decay process. It elucidates an efficient charge transfer of the $MAPbI_2Br/TiO_2$ interface. Meanwhile, $MAPbI_2Br$ presents prolonged charge carrier lifetime compared to $MAPbI_3$ as shown in Fig. 2c, indicating an improved charge carrier transport property of $MAPbI_2Br$.[18,19] The improvement might be associated with its highly ordered cubic structure, whereas, in comparison, the tetragonal structure of $MAPbI_3$ is less ordered.

Fig. 3a shows the photocurrent density-photovoltage (J-V) curves of the mesoscopic perovskite devices under standard AM 1.5G illumination at 100 mW cm^{-2}. The photovoltaic parameters, open circuit voltage (V_{OC}), fill factor (FF), short circuit current density (J_{SC}) and PCE are tabulated in Table 1. Encouragingly, the $MAPbI_2Br$-based device displayed a short-circuit current density (J_{SC}) of 15.37 mA cm^{-2}, a fill factor (FF) of 0.69, an open-circuit voltage (V_{OC}) of 1.04 V, amounting to a PCE of 11.03%, which is the highest value observed for solid state $MAPbI_2Br$-based devices to date. For comparison, the device based on $MAPbI_3$ was also fabricated under the same conditions and showed a power conversion efficiency of 10.51% with a short-circuit current density (J_{SC}) of 17.36 mA cm^{-2}, an open-circuit voltage (V_{OC}) of 0.904 V and a fill factor (FF) of 0.67. Comparison of the V_{OC} value of $MAPbI_3$-based device with that of $MAPbI_2Br$-based device shows that photovoltage can be increased from 0.904 V to 1.04 V simply by changing the perovskite material from $MAPbI_3$ to $MAPbI_2Br$ in the same device structure. To further check the reproducibility of device performance, Fig. S3 shows the statistic of the V_{OC} for a batch of 15 devices based on $MAPbI_2Br$ and $MAPbI_3$. Obviously, the average V_{OC} value for the devices with $MAPbI_2Br$ is 1.03 V, which is much higher than that of the $MAPbI_3$ one at 0.903 V. The $MAPbI_2Br$, with a wider band gap (~1.77 eV) than $MAPbI_3$ (1.55 eV), has a higher conduction band edge (CB, -3.6 eV) as compared to $MAPbI_3$ (CB, -3.9 eV).[28] The origin of V_{OC} in perovskite solar cells is typically described by the difference between the conduction band minimum of the perovskite and the HOMO of the HTM, or by the potential difference between the quasi-Fermi level of the electron (E_{fn}) at the electron extracting layer/anode interface and the quasi-Fermi level of the hole (E_{fp}) at the hole extracting layer/cathode interface under illumination, assuming that recombination within the device can be ignored.[29,30] Therefore, when E_{fn} and E_{fp} are built-up within the device under light illumination, $MAPbI_2Br$ might lead to a larger difference between E_{fn} and E_{fp} as compared to $MAPbI_3$, in spite of using the same electron (TiO_2) extracting layer, thus resulting in a higher Voc. This result is in accordance with the reports that the perovskite materials contribute to E_{fn} and E_{fp} within the device.[30] In addition, it is noted that the V_{OC} (around 1.1 V) of the device is almost equal to the energy gap (around 1.1 eV) between the TiO_2 CB (~-3.9 eV) and the work function of carbon CE (~-

5.0 eV), indicating that an ohmic contact is formed between the counter electrode with the perovskite layer in this architecture. Thus the V_{OC} is mainly determined by the potential difference between the quasi-Fermi level of the electron (E_{fn}) at the electron extracting layer/anode interface and the quasi-Fermi level of the hole (E_{fp}) at the hole extracting layer/cathode interface under illumination as described before.

The reduction of J_{sc} with $MAPbI_2Br$ perovskite is directly related to the blue shift of absorption onset, as indicated from the IPCE spectra in Fig. 3b. Consistent with the larger bandgap, the onset of the IPCE spectra blue shifted from 800 nm for the $MAPbI_3$ to ~700 nm for the $MAPbI_2Br$ perovskite. As shown in Fig. 3b, the $MAPbI_2Br$-based device shows a wide range photocurrent response with IPCE over 60% from 350 nm to 600 nm and a maximum IPCE approaching 80% around 400 nm to 500 nm. The IPCE value shown in the spectra is in good agreement with the absorption spectra of $MAPbI_2Br$ as shown in Fig. 1b. It is noted that the $MAPbI_2Br$-based photovoltaic cell gives higher incident photon-to-current conversion efficiency (IPCE) values at 400-600 nm than those of $MAPbI_3$ as can be seen from Fig. 3b, although the $MAPbI_3$-based device presents a broader IPCE performance in the range from 400 nm to 800 nm. This superior performance of $MAPbI_2Br$ is considered to stem from the high absorption coefficient in visible light region together with its prolonged charge carrier lifetime.[18,31] Here it is observed that the improvement in the short-circuit current for the $MAPbI_3$-based device is accompanied by a larger open-circuit voltage relative to $MAPbI_2Br$-based device. In addition, as demonstrated by the dark current-voltage curves in Fig. S4, devices based on $MAPbI_2Br$ perovskite showed much higher dark current onset as compared to the devices fabricated with $MAPbI_3$ perovskite. This is indicative of an effectively inhibited charge recombination in the former case.

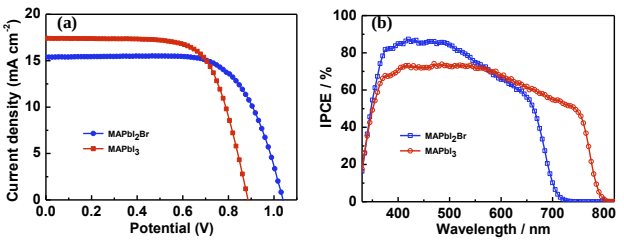

Fig. 3 (a) Current density-voltage (J-V) curves for devices of TiO_2/Al_2O_3/carbon($MAPbI_2Br$) configuration and TiO_2/Al_2O_3/carbon ($MAPbI_3$) under 1 sun illumination (100mW cm^{-2}). (b) The corresponding IPCE for the two devices.

Table 1 Photovoltaic properties of TiO_2/Al_2O_3/carbon($MAPbI_2Br$) and TiO_2/Al_2O_3/carbon($MAPbI_3$) devices.

Device	J_{sc} [mAcm^{-2}]	V_{oc} [V]	FF	PCE [%]
TiO_2/Al_2O_3/C($MAPbI_2Br$)	15.37	1.04	0.69	11.03
TiO_2/Al_2O_3/C($MAPbI_3$)	17.36	0.904	0.67	10.51

As shown in Fig. 4a, the relationship between the J_{SC} of the solar cell based on $MAPbI_2Br$ and different light intensities was investigated. Obviously, good linearity is observed for the $MAPbI_2Br$-based device, indicating that the charge collection is independent with light density. In Fig. 4b, the open circuit voltage as a function of ln(I) is plotted where I is the incident light intensity. From the relationship between $\delta V_{OC} \sim \ln(I)$, the slope of the fitting curve is 0.054, close to 0.052 ($2\kappa T/q$), κ is the Boltzmann coefficient, T is the absolute temperature, indicating that the main recombination mechanism in the device is free carrier recombination. According to previous investigation, it is supposed that there is no obvious space-charge limit in the TiO_2/Al_2O_3/carbon(perovskite) junction due to small difference in the mobility between electrons and holes. Fig. S5 illustrates the current-voltage (J-V) characteristics of a typical TiO_2/Al_2O_3/carbon ($MAPbI_2Br$) cell measured under light intensities of 96.6, 69.2, 43.5 and 24.7 mW cm^{-2}. The short-circuit current density (J_{SC}), open-circuit voltage (V_{OC}) and fill factor (FF), respectively, are 15.01 mA cm^{-2}, 1.08 V and 0.66, which lead to a power-conversion efficiency of 10.74% measured at 96.6 mW cm^{-2}. At 69.2, 43.5 and 24.7 mW cm^{-2} the device exhibited very similar efficiencies, 10.72%, 10.69% and 10.71%, respectively.

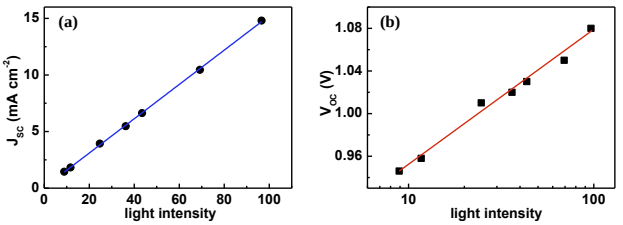

Fig. 4 (a) The short circuit current (J_{SC}) and (b) open circuit voltage (V_{OC}) of TiO_2/Al_2O_3/carbon($MAPbI_2Br$) solar cell as function of light intensity.

Anomalous hysteresis in the J-V curves of perovskite solar cells has been widely observed, which is predominantly arises from the presence of the perovskite absorber and dependent on the device architecture.[32,33] We therefore recorded the J-V curves of TiO_2/Al_2O_3/carbon($MAPbI_2Br$) cells with different scanning directions (Fig. 5). For such device, there is only a small change in the relative scale of the hysteresis with changing scan rate from 0.03 to 0.5 V/s, revealing a weak scan-rate dependence of the hysteresis effect. We conclude that a minor hysteresis exist in the J-V curves of TiO_2/Al_2O_3/carbon($MAPbI_2Br$) cell, which ascribe to the complication reasons that the contact interfaces in the device structure and chemical or structural changes in the perovskite are assumed to have a big effect on the extent of hysteresis.[34,35]

In addition, measuring the steady-state power output directly at a given forward bias is also a feasible means to estimate the power conversion efficiency.[36] As shown in Fig. 6, we recorded the photocurrent density of $MAPbI_2Br$-based device held at a forward bias of 0.76 V near their maximum output power point as a function of time to monitor the stabilized power output under working conditions. For the $MAPbI_2Br$-based device, the photocurrent density stabilizes within seconds to approximately 14.3 mA cm^{-2}, yielding the stabilized power conversion efficiency around 10.9% measured after 300 s. This indicates that the test condition (from forward bias to short circuit scans with a scanning rate of 0.07 V/s) provides an accurate representation of the cells photovoltaic performance.

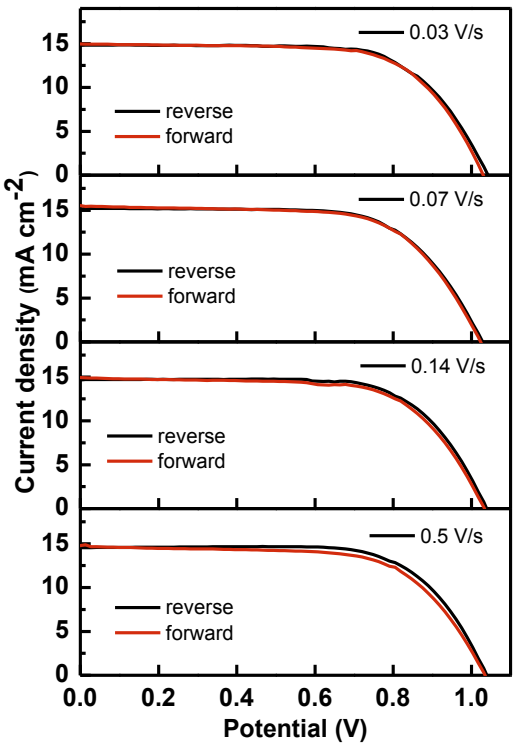

Fig. 5 Influence of scanning conditions on J-V curves of TiO_2/Al_2O_3/carbon($MAPbI_2Br$) solar cell. From forward bias to short circuit (reverse) and from short circuit to forward bias (forward) cell measured under simulated AM1.5 100 mW cm^{-2} sun light at a range of scan rates from 0.03 to 0.5 V/s.

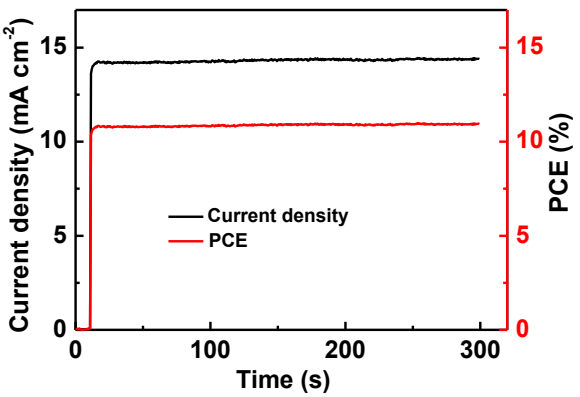

Fig. 6 Photocurrent density and PCE as a function of time for the TiO_2/Al_2O_3/carbon($MAPbI_2Br$) device held at a forward bias of maximum output power point (0.76 V). The cell was placed in the dark prior to the start of the measurement.

The issue of stability is another critical concern for perovskite photovoltaic devices. The major factor affecting the stability of PSCs may largely attribute to the decomposition of the perovskite when exposed to moisture. Under ambient air condition with regular humidity of 50%, $MAPbI_2Br$ is much more stable than $MAPbI_3$,[19] which we can also easily identify by the colour change of the films in Fig. S6. Thus, the $MAPbI_2Br$ devices are expected to have better stability than those with $MAPbI_3$. Here, the stability test of the $MAPbI_2Br$ devices was carried out in ambient atmosphere at room temperature, that is, the unsealed devices were subjected to constant light soaking at a relatively low light intensity of about 25 mW cm^{-2} using white light emitting diodes. As shown in Fig. 7, the stability test indicates that the efficiency of the $MAPbI_2Br$ devices is well retained after exposing for 300 h in air without any encapsulation. The J_{SC} has shown an initial value at nearly 14.5 mA cm^{-2} and been stabilized at 15.0 mA cm^{-2}. During the stability test, the V_{OC} is a little increased to 1.05 V, while FF remained similar at around 0.67. Therefore, the stability performance of these devices is considered to be fairly good in practical consideration. Moreover, the results show that the PCE improvement of the perovskite solar cells with time in the first several days after fabrication, which demonstrate high stability and is in good agreement with the literature.[24] The possible reason may be associated with the interface state between the perovskite layer and carbon CE. However, the detailed mechanism is still not clear and needs to be further investigated.

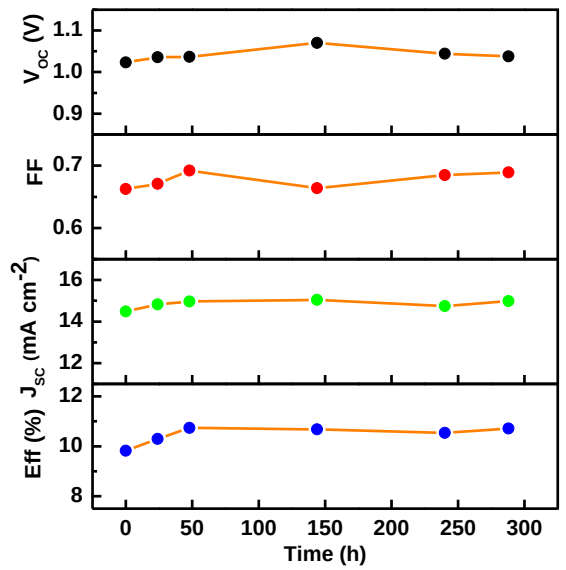

Fig. 7 Stability of TiO_2/Al_2O_3/carbon($MAPbI_2Br$) solar cells subjected to light soaking using white light emitting diodes (25 mW cm^{-2}) at room temperature without encapsulation.

Conclusions

In summary, we have successfully fabricated HTM-free mesoscopic PSC devices using $CH_3NH_3PbI_2Br$ as light absorber and hole conductor. The optimized device has achieved a power conversion efficiency of 11.03% with V_{OC} of 1.04 V and FF of 0.69. Compared to the $CH_3NH_3PbI_3$, the incorporation of bromine in mixed halide perovskite led to a phase transition with a larger bandgap and longer charge carrier lifetime, which is beneficial to the enhancement of V_{OC} and the stability against humidity in air. This cell architecture is constructed with inorganic metal oxides in combination with carbon CE by full printable techniques. Therefore, this work paves the way to realize low cost, large-scale, and highly efficient hybrid photovoltaic cells.

Acknowledgement

The Financial support from the Director Fund of the WNLO, the

973 Program of China (2014CB643506, 2013CB922104, and 2011CBA00703), and the NSFC (21161160445, and 21173091), and the Fundamental Research Funds for the Central Universities (HUST: CXY12Q022) is acknowledged. The authors thank the Analytical and Testing Centre of Huazhong University of Science & Technology and the Center of Micro-Fabrication and Characterization (CMFC) of WNLO for the measurements of the samples.

Notes and references

[a] *Grätzel Center for Mesoscopic Solar Cells, Wuhan National Laboratory for Optoelectronics, Huazhong University of Science and Technology, Luoyu Road 1037, Wuhan 430074, P. R. China, E-mail: mingkui.wang@mail.hust.edu.cn*

[b] *Department of Materials Engineering, Monash University, Melbourne, Australia*

† Electronic Supplementary Information (ESI) available: [Photoluminescence, photovoltaic performace, and optical imapges of different devices]. See DOI: 10.1039/b000000x/

1. H. Kim, C. Lee, J. Im, K. Lee, T. Moehl, A. Marchioro, S. Moon, R. Humphry-Baker, J. Yum, J. Moser, M. Gratzel and N. G. Park, *Sci. Rep*., 2012, **2**.
2. H. Snaith, *J. Phys. Chem. Lett.*, 2013, **4**, 3623-3630.
3. M. Gratzel, *Nat Mater*, 2014, **13**, 838-842.
4. http://www.nrel.gov/ncpv/images/efficiency_chart.jpg
5. N. Park, *J. Phys. Chem. Lett.*, 2013, **4**, 2423-2429.
6. G. Xing, N. Mathews, S. Sun, S. Lim, Y. M. Lam, M. Grätzel, S. Mhaisalkar and T. Sum, *Science*, 2013, **342**, 344-347.
7. J. Cui, F. Meng, H. Zhang, K. Cao, H. Yuan, Y. Cheng, F. Huang and M. Wang, *ACS Appl. Mater. Interfaces*, 2014, **6**, 22862-22870.
8. J. Ball, M. Lee, A. Hey and H. Snaith, *Energy Environ. Sci.*, 2013, **6**, 1739-1743.
9. S. Stranks, G. Eperon, G. Grancini, C. Menelaou, M. Alcocer, T. Leijtens, L. Herz, A. Petrozza and H. Snaith, *Science*, 2013, **342**, 341-344.
10. C. Wehrenfennig, G. Eperon, M. Johnston, H. Snaith and L. Herz, *Adv. Mater*., 2014, **26**, 1584-1589.
11. S. Colella, E. Mosconi, P. Fedeli, A. Listorti, F. Gazza, F. Orlandi, P. Ferro, T. Besagni, A. Rizzo and G. Calestani, *Chem. Mater.*, 2013, **25**, 4613-4618.
12. E. Edri, S. Kirmayer, M. Kulbak, G. Hodes and D. Cahen, *J. Phys. Chem. Lett.*, 2014, **5**, 429-433.
13. A. Sadhanala, F. Deschler, T. Thomas, S. Dutton, K. Goedel, F. Hanusch, M. Lai, U. Steiner, T. Bein and P. Docampo, *J. Phys. Chem. Lett.*, 2014, **5**, 2501-2505.
14. E. Hoke, D. Slotcavage, E. Dohner, A. Bowring, H. Karunadasa and M. McGehee, *Chem. Sci.*, 2015, **6**, 613-617.
15. S. Kazim, M. Nazeeruddin, M. Grätzel and S. Ahmad, *Angew. Chem. Int. Edit.*, 2014, **53**, 2812-2824.
16. J. Noh, S. Im, J. Heo, T. Mandal and S. Seok, *Nano lette.*, 2013, **13**, 1764-1769.
17. S. Kulkarni, T. Baikie, P. Boix, N. Yantara, N. Mathews and S. Mhaisalkar, *J. Mater. Chem. A*, 2014, **2**, 9221-9225.
18. J. Qiu, Y. Qiu, K. Yan, M. Zhong, C. Mu, H. Yan and S. Yang, *Nanoscale*, 2013, **5**, 3245-3248.
19. M. Zhang, M. Lyu, H. Yu, J. H. Yun, Q. Wang and L. Wang, *Chem-Eur. J.*, 2015, **21**, 434-439.
20. E. Edri, S. Kirmayer, D. Cahen and G. Hodes, *J. Phys. Chem. Lett.*, 2013, **4**, 897-902.
21. Y. Zhao and K. Zhu, *J. Am. Chem. Soc.*, 2014, **136**, 12241-12244.
22. Y. Zhao and K. Zhu, *J. Phys. Chem. C*, 2014, **118**, 9412-9418.
23. X. Xu, H. Zhang, K. Cao, J. Cui, J. Lu, X. Zeng and M. Wang, *ChemSusChem*, 2014, **7**, 3088-3094.
24. A. Mei, X. Li, L. Liu, Z. Ku, T. Liu, Y. Rong, M. Xu, M. Hu, J. Chen, Y. Yang, M. Graetzel and H. Han, *Science*, 2014, **345**, 295-298.
25. F. Hao, C. Stoumpos, Z. Liu, R. Chang and M. Kanatzidis, *J. Am. Chem. Soc.*, 2014, **136**, 16411-16419.
26. Z. Liu, M. Zhang, X. Xu, L. Bu, W. Zhang, W. Li, Z. Zhao, M. Wang, Y. Cheng and H. He, *Dalton Trans*., 2015, DOI: 10.1039/C4DT02904F.
27. Z. Wei, K. Yan, H. Chen, Y. Yi, T. Zhang, X. Long, J. Li, L. Zhang, J. Wang and S. Yang, *Energy Environ. Sci.*, 2014, **7**, 3326-3333.
28. A. Kojima, K. Teshima, Y. Shirai and T. Miyasaka, *J. Am. Chem. Soc.*, 2009, **131**, 6050-6051.
29. B. Cai, Y. Xing, Z. Yang, W. Zhang and J. Qiu, *Energy Environ. Sci.*, 2013, **6**, 1480-1485.
30. S. Ryu, J. Noh, N. Jeon, Y. Kim, W. Yang, J. Seo and S. Seok, *Energy Environ. Sci.*, 2014, **7**, 2614-2618.
31. M. Zhang, H. Yu, M. Lyu, Q. Wang, J. Yun and L. Wang, *Chem. Commun.*, 2014, **50**, 11727-11730.
32. H. Kim and N. Park, *J. Phys. Chem. Lett.*, 2014, **5**, 2927-2934.
33. H. Snaith, A. Abate, J. Ball, G. Eperon, T. Leijtens, N. Noel, S. Stranks, J. Wang, K. Wojciechowski and W. Zhang, *J. Phys. Chem. Lett.*, 2014, 5, 1511-1515.
34. H. Chen, N. Sakai, M. Ikegami and T. Miyasaka, *J. Phys. Chem. Lett.*, 2015, **6**, 164-169.
35. J. Wei, Y. Zhao, H. Li, G. Li, J. Pan, D. Xu, Q. Zhao and D. Yu, *J. Phys. Chem. Lett.*, 2014, **5**, 3937-3945.
36. M. Xiao, F. Huang, W. Huang, Y. Dkhissi, Y. Zhu, J. Etheridge, A. Gray-Weale, U. Bach, Y. Cheng and L. Spiccia, *Angew. Chem. Int. Edit.*, 2014, **126**, 10056-10061.

